# Reconstructing the digital twin of forests from a 3D library: quantifying trade-offs for radiative transfer modeling

**Chang Liu[a,*], Kim Calders[a], Niall Origo[b,c], Mathias Disney[b,d], Félicien Meunier[a], William Woodgate[e,f], Jean-Philippe Gastellu-Etchegorry[g], Joanne Nightingale[h], Eija Honkavaara[i], Teemu Hakala[i], Lauri Markelin[i], Hans Verbeeck[a]**

[a]CAVELab - Computational & Applied Vegetation Ecology, Department of Environment, Ghent University, Belgium

[b]Department of Geography, University College London, London WC1E 6BT, UK

[c]Climate and Earth Observation Group, National Physical Laboratory, Teddington TW11 0LW, UK

[d]NERC National Centre for Earth Observation (NCEO), University College London, London WC1E 6BT, UK

[e]School of Earth and Environmental Sciences, The University of Queensland, Brisbane, 4072, Australia

[f]Space and Astronomy, CSIRO, Kensington, WA, 6151, Australia

[g]Toulouse III University, CESBIO - CNES, CNRS, IRD, INRAE, Toulouse, France

[h]WWF-UK, Woking, Surrey GU21 4LL, UK

[i]Department of Remote Sensing and Photogrammetry, Finnish Geospatial Research Institute, National Land Survey of Finland, Finland

* Correspondence: Chang Liu (Chang.Liu@UGent.be)

# Abstract

Radiative transfer models that use spatially explicit 3D models to represent forest structure can simulate highly realistic Earth Observation (EO) data. Such simulations at the forest stand scale (≥ 1-ha) allow for more direct calibration and validation of EO products. Explicitly reconstructing 3D forest structures at scales that can be compared directly with satellite EO data (i.e., dozens to hundreds of meters) is challenging. Reconstructing large forest areas (≥ 1-ha) using a representative subset (i.e., forest subsampling) is a potentially more practical and feasible method. However, the impacts of forest subsampling on radiative transfer (RT) modeling were never formally tested in the spatially explicit forest scene.

This study quantified the trade-offs involved in two main subsampling approaches when reconstructing the spatially explicit scene of a real forest for RT modeling. The two subsampling approaches were: (1) subplot subsampling - area-based, using the subplot (i.e. a fixed area) as the basic sampling and reconstruction unit; and (2) tree library subsampling - tree-based, using the individual tree as the basic sampling and reconstruction unit. We used the Discrete Anisotropic Radiative Transfer Model (DART) to simulate the Bidirectional Reflectance Factor (BRF) of the completely reconstructed 1-ha 3D-explicit forest scene, as well as the simplified forest scenes built from various subsets of the same forest. The simulated reflectance deviation of the simplified forest scenes was evaluated by comparing it with the fully reconstructed forest scene.

The results showed that for subplot subsampling, as the sampling fraction increased from 10% to 90%, the normalized mean BRF deviation of radiative transfer simulations decreased from -2.7% to -0.0034% and its standard deviation decreased from 7.7% to 0.54%. Additionally, as the sampling fraction increased from 10% to 90%, the normalized mean BRF deviation of tree library subsampling decreased from -7.4% to -1.3% and its standard deviation decreased from 2.8% to 0.51%.

Overall, sampling 20% of the forest area using the subplot subsampling method was an effective reconstruction strategy for the temperate deciduous forest. This strategy ensured a normalized mean BRF deviation of -2.9% and a standard deviation of 3.7% in the forest stand studied, with a relatively low reconstruction effort.

This study shows that the forest subsampling approach allows for reconstructing 3D-explicit forest scenes for RT modeling at the forest stand scale (≥ 1-ha). Accordingly, highly realistic EO data can be

modeled at the forest stand scale, which allows for more direct calibration and validation of EO products.

**Keywords:** radiative transfer; forest 3D reconstruction; canopy structure; forest subsampling; sampling fraction; terrestrial laser scanning.

# 1 Introduction

Spatial and temporal information on essential climate variables in forest ecosystems can be obtained through remote sensing (RS) (Bojinski et al., 2014). However, RS cannot directly measure most forest properties of interest for environmental applications (e.g., leaf area index, fraction of absorbed photosynthetically active radiation, biomass, and net primary productivity). Instead, these properties must be inferred from the observed reflected, emitted, or scattered radiation through mathematical or empirical modeling. In this context, a proper understanding of the interaction between light (i.e., electromagnetic radiation) and forest structure is essential for vegetation RS interpretation and product development (Gastellu-Etchegorry et al., 2012).

Physically-based Radiative transfer Models (RTMs) can simulate the interaction between light and forest structure (Widlowski et al., 2014, 2013). This can help us better understand the nature of light transmission within forests, as well as interpret RS data. Therefore, RTMs often underpin the retrieval of biophysical parameters from Earth Observation data. RTMs are also of great significance for improving the calibration and validation of RS products with ground data. Furthermore, RTMs allow detailed quantification of light regimes (scattering and absorption) within canopies. This can provide information relevant to study key ecosystem processes such as photosynthesis and transpiration.

One of the critical inputs for RTMs is the representation of forest structure. Forest structure is the three-dimensional arrangement of trees and other plants, in combination with nonliving spatial elements such as soils and slopes (Seidler, 2017). More specifically, the position, shape, size, and orientation of every single object (e.g., leaf, branch, stem, etc.) in the canopy define all together the forest structure (Calders et al., 2020b; Ross, 1981). The representation of forest structure impacts the performance of RTMs (Janoutová et al., 2019; Li et al., 2018; Liu et al., 2022; Widlowski et al., 2014; Van der Zande et al., 2011). More accurate radiative transfer (RT) simulations and more physically-realistic parameter inversions can be obtained if RTMs use more accurate 3D forest structure representations.

3D-explicit forest models (Calders et al., 2018) are more physically realistic structure representations than the commonly used turbid medium forest structure representations (e.g., voxel-based (Schneider et al., 2014) or layer-based (Jacquemoud et al., 2009) structural models). 3D-explicit forest models first use geometric 3D models to reconstruct every single branch and stem representing their structure in the real world. These woody components are then used as attractors to reconstruct

leaves using the field-measured structural properties and geometric 3D models (Calders et al., 2018). However, forests have highly complex 3D structures. 3D-explicit reconstruction of forest structure at the forest stand scale (> 1-ha) requires a tremendous amount of structural information (Åkerblom & Kaitaniemi, 2021; Disney, 2019; Widlowski et al., 2014), including the position, shape, size, and orientation of every stem and branch. Collecting this structural information and conducting reconstruction at the forest stand scale is time- and labor-intensive, or even impossible (Åkerblom & Kaitaniemi, 2021; Disney, 2019).

Reconstructing the entire forest by using a representative subset of the forest such as trees or subplots (i.e. forest subsampling) is a potentially more practical and feasible method. Previous studies have used subsampling methods to reconstruct 3D-explicit forests because of the laborious nature of forest stand reconstructions (Côté et al., 2018, 2012, 2009; Janoutová et al., 2019; Widlowski et al., 2015, 2014). In the forest subsampling method, a few trees or a subplot in the forest stand are reconstructed explicitly in 3D and the forest stand is then reconstructed by replicating this subset multiple times. With this subsampling method, we can easily increase the spatial scale of the reconstructed forest scene to match the scale of possible applications (e.g., understanding forest RT processes, retrieval algorithm development, sensor design, or RS calibration and validation activities).

However, forest subsampling for RT modeling relies on the assumption that the canopy structure of a large area can be accurately captured from artificially assembling and repeating a limited number of constitutive elements captured and reconstructed at a smaller scale, and therefore minimally impacts the RT modeling. To the best authors' knowledge, this hypothesis was never formally tested. Given the availability of more and more high-quality terrestrial laser scanning (TLS) data, there is an increased potential for using 3D measurements to develop hectare-scale canopy RT models (Calders et al., 2020a). Therefore, there is a need to quantify the RT deviation caused by forest subsampling methods. Until recently (Calders et al., 2018), complete and realistic forest scenes with 3D-explicitly reconstructed structure did not exist, preventing such quantification.

In this study, for the first time, we used the fully 3D-explicit scene of a real forest stand to test the impact of forest subsampling on RT modeling, using the complete 1-ha 3D-explicit forest scene of Wytham Woods (Calders et al., 2018). This study quantified the deviation in simulated reflectance resulting from varying degrees of subsampling a typical closed-canopy temperate deciduous forest scene in RT modeling; and determined the optimal subsampling strategy to build large-scale 3D-explicit

forest scenes for RT modeling. Since UAV is a useful close-range RS method to collect high-resolution imagery for forest health, thinning, structure, and fire monitoring, the assessed performance of the 3D-explicit RT modeling of the complete 1-ha forest scene was benchmarked against a UAV reflectance dataset.

# 2 Materials and methods

## 2.1 Study area

The study site is located in Wytham Woods, a typical temperate forest site in southern Great Britain (Kirby et al., 2014; Savill et al., 2011). The study site is a 1-ha (100 × 100 m) plot of mixed deciduous forest, nested within an 18-ha long-term forest inventory plot run by Oxford University and is part of the ForestGEO global network of forest inventory plots (Calders et al., 2018, 2022). The mean annual temperature and precipitation are 10 °C and 729 mm, respectively (Butt et al., 2009). In the studied plot, there were 550 standing trees in 2015/16. Sycamore (*Acer pseudoplatanus*), common ash (*Fraxinus excelsior*), and common hazel (*Corylus avellana*) were the dominant tree species in the study area (Table 1).

**Table 1** Tree species and structural information of the 1-ha forest stand. The diameter at breast height (DBH) and tree height are from the forest inventory. Species name colors are used to aid subsequent figure interpretation.

| Tree species | | Number | Diameter at breast height (cm) | | Tree height (m) | |
|---|---|---|---|---|---|---|
| | | | Average value | Standard deviation | Average value | Standard deviation |
| Sycamore (*Acer pseudoplatanus*) | Live | 362 | 23.7 | 17.6 | 16.4 | 6.2 |
| | Dead | 16 | 12.9 | 18.9 | 6.5 | 4.8 |
| Common ash (*Fraxinus excelsior*) | Live | 51 | 22.3 | 22 | 15.6 | 7.5 |
| | Dead | 1 | 5.5 | / | 5.9 | / |
| English oak (*Quercus robur*) | Live | 22 | 64.7 | 16.1 | 20.4 | 3.4 |
| | Dead | 1 | 66.7 | / | 16.6 | / |
| Common hazel (*Corylus avellana*) | Live | 33 | 9.1 | 2.7 | 8.5 | 2.4 |
| | Dead | 2 | 4 | 4.9 | 1.3 | 0.5 |
| Common hawthorn (*Crataegus monogyna*) | Live | 16 | 9.7 | 3.5 | 7.7 | 2.6 |
| | Dead | 3 | 9.9 | 5.3 | 6.9 | 4.7 |
| Field maple (*Acer campestre*) | Live | 2 | 7.8 | 0.98 | 7.4 | 1.2 |
| Unknown | Live | 34 | 7.5 | 3.2 | 7.1 | 3.4 |
| | Dead | 7 | 9.8 | 10.6 | 4.6 | 3.4 |
| **Total** | | 550 | 23.7 | 17.6 | 16.4 | 6.2 |

## 2.2 Data collection

### 2.2.1 Forest structural and spectral data

The 3D structural information of trees and the digital elevation model were collected by a RIEGL VZ-400 terrestrial laser scanner. The TLS data were collected in both leaf-on (June and July 2015) and leaf-off (December 2015 and January 2016) conditions for 3D reconstruction (Calders et al., 2018). The complete TLS scan was conducted at a 6-ha area. The 6-ha area was divided into 20 x 20 m$^2$ grids, which means there were TLS scans every 20 m. In total, there were 176 scan locations. On each location two scans were conducted (one vertical and one horizontal) to get a better field of view and less occlusion, especially for top of canopy. And a 1-ha plot in the middle of the 6-ha area was used for further reconstruction and radiative transfer modeling. The angular sampling was 0.04° for both zenith and azimuth angles. The zenith range of scanning was 0°-130°, and the azimuth range was 0°-360°.

A FieldSpec (ASD Spectrometer) was used to collect the spectral properties of leaves, bark, and understorey. The spectral properties of the leaves and bark were measured for each tree species. Twenty-seven trees were measured in total, and the number of sampled individuals for each tree species was based on their relative abundance in the plot. Ten leaves from two branches were measured for each tree. The spectral properties of the bark were measured using the ASD contact probe attached to the ASD Spectrometer. The understorey reflectance was measured using the bare fiber and pistol grip attachment of ASD Spectrometer. We divided the one-hectare plot into 25 grids of 20 × 20 m. A white reference panel measurement was taken for every five grids. In the middle of each grid, five samples were taken. The final understorey reflectance was the average value of all measurements. A detailed description of this data collection can be found in Calders et al. (2018).

## 2.2.2 UAV image dataset

Hyperspectral UAV images of the same 1-ha area in Wytham Woods were collected on 30 June 2015. A 2D format hyperspectral camera based on tunable Fabry-Pérot Interferometer (FPI) (camera prototype 2012b) was used to collect images (Honkavaara et al., 2013; Saari et al., 2013). The image size was 1024 × 648 pixels with a pixel size of 11 μm and the focal length was 9 mm. The camera was spectrally calibrated (Hakala et al., 2018). The platform was a hexacopter UAV with Tarot 960 foldable frame and Pixhawk autopilot. The data was captured from 09:46 to 10:04 (local time) in the morning, the conditions were cloud free, and the sun zenith and azimuth angles were 38.4° and 125.2°, respectively. The nominal flight height was 90 m and the distance from the sensor to the canopy was about 70 m, resulting in a ground sample distance of 9-11 cm. The dataset was collected as an image block with forward and side overlaps at the tree top level of 71% and 64%. The camera had a 2D format imaging geometry with a field of view (FOV) of ±18° in the flight direction, ±27° in the cross-flight direction, and ±31° at the format corner. The hyperspectral image exterior orientations were calculated using the custom method for FPI images (Honkavaara et al., 2017). The images were orthorectified using the image orientations and digital surface model. Bidirectional Reflectance Factor (BRF) mosaics were calculated utilizing the most-nadir method with a 20 cm ground sample distance (i.e., the spatial resolution of the images was 20 cm) using an in-house software (Honkavaara et al., 2013); pixels were calculated as averages from four pixels. BRF is the ratio of reflected radiant flux from the surface to the reflected radiant flux from an ideal diffuse reference panel for specific incidents and viewing

cases. Images of 32 wavebands whose central wavelength ranged from 520 nm to 886 nm were used in this study (Table A1). The radiance-to-reflectance transformation was carried out using the direct method utilizing the irradiance data collected on ground and onboard the drone. A detailed description of the data collection and processing can be found in Hakala et al. (2018).

## 2.3 3D-explicit reconstruction of forest stand

The complete 1-ha forest stand was 3D-explicitly reconstructed based on the structural and spectral data collected by Calders et al. (2018) (Figure 1). Every tree was explicitly reconstructed individually. The reconstructed 3D-explicit model was made of solid facets with shapes and sizes similar to the real objects they represent. The stems and branches were reconstructed as cylinders, further converted to hexagonal prisms for radiative transfer modeling. The leaves were reconstructed as tetragons (Figure A1) (Calders et al., 2018). The reconstructed leaf shape was selected as a trade-off between simulation realism and run time efficiency. The stems and branches were built using Quantitative Structural Models (QSMs) (Calders et al., 2015) fitted to the point cloud data obtained by TLS. Then the leaves were reconstructed by the Foliage and Needles Naïve Insertion (FaNNI) algorithm (Åkerblom et al., 2018) and were added to the tree QSM structure. Finally, the 3D tree models were put on the digital elevation model (DEM) to reconstruct the 3D-explicit structure of the complete 1-ha forest stand. The spectral properties of leaves, stems, and branches were assigned based on the six tree species in the site and the in-situ measured spectral data (Figure A2ab). The in-situ measured understorey reflectance was used as the reflectance of the DEM (Figure A2c).
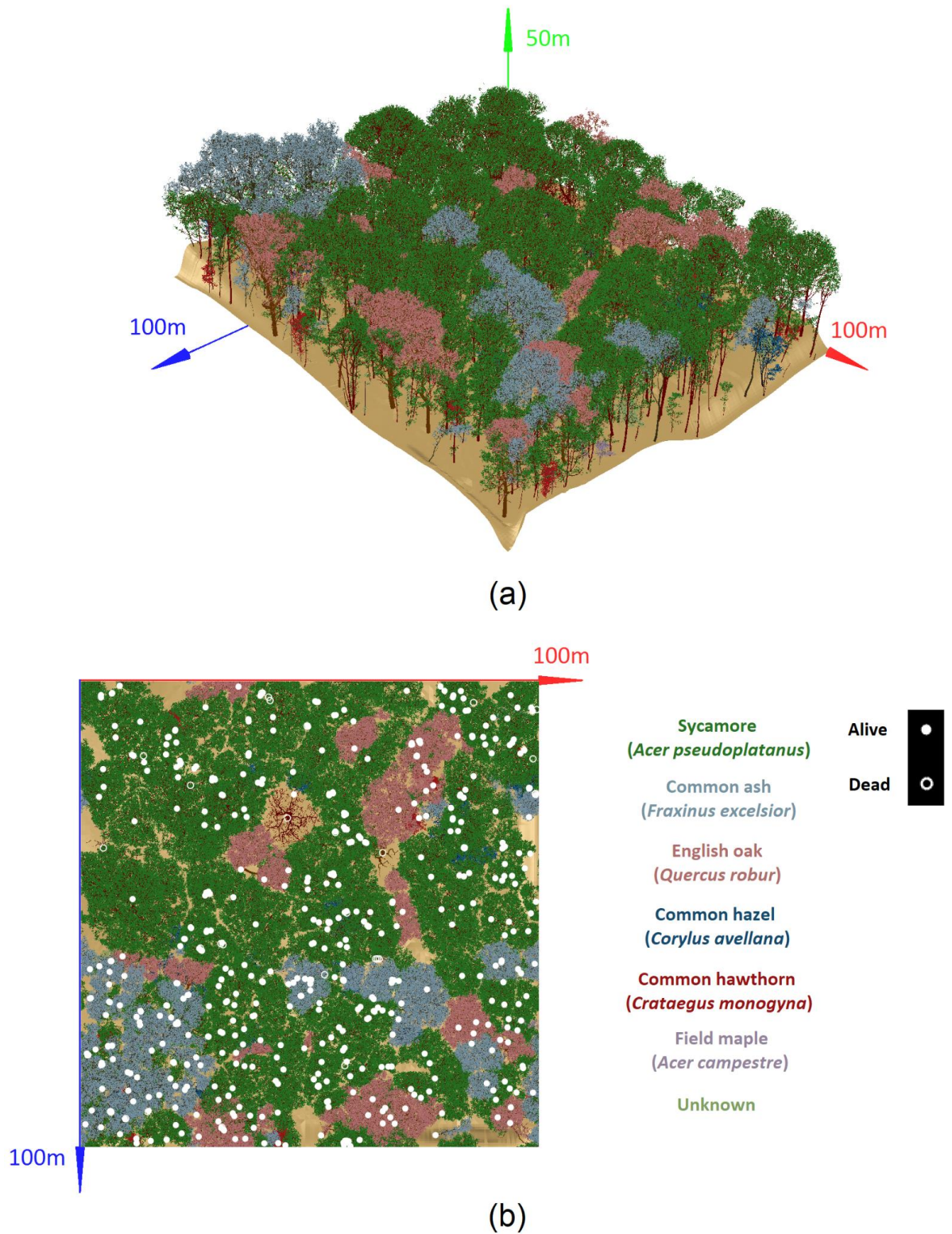
**(a)**



Sycamore (*Acer pseudoplatanus*)

Common ash (*Fraxinus excelsior*)

English oak (*Quercus robur*)

Common hazel (*Corylus avellana*)

Common hawthorn (*Crataegus monogyna*)

Field maple (*Acer campestre*)

Unknown

Alive

Dead

**(b)**

**Figure 1.** The 3D-explicit model of the complete 1-ha forest stand (Calders et al., 2018). The different leaf colors represent the different tree species present in Wytham Woods. The markers in subfigure (b) represent the stem location of trees.

## 2.4 Forest subsampling methods

Two methods were tested to subsample the complete 1-ha forest stand, hereafter referred to as the "subplot" and the "tree library" subsampling methods (Côté et al., 2009; Janoutová et al., 2019; Widlowski et al., 2015, 2014). Different sampling fractions were also tested. For the subplot subsampling method, the sampling fraction was the reconstructed subplot area divided by the area of the complete forest stand (1-ha). For the tree library method, the sampling fraction was the number of reconstructed trees divided by the total number of trees in the complete 1-ha forest stand (550 trees).

## 2.4.1 Subplot subsampling method (area based)

This method utilizes a subplot to represent the entire forest stand (Figure 2a). A subplot is defined as a plot randomly nested in the complete 1-ha forest stand. In this study, we tested subplot sizes from 1000 m$^2$ to 9000 m$^2$ with an interval of 1000 m$^2$, equivalent to a sampling fraction varying from 10% to 90% with 10% increments. To quantify the uncertainty of the subplot subsampling method, we tested 100 randomly located subplots for each subplot size. A total of 900 subplots were therefore tested (9 subplot sizes x 100 subplots/size). Only trees with stem base positions within the subplot were used in the subplot. If parts of these trees (e.g. crown or branches) were outside the subplot, this part was replicated on the other side of the subplot.
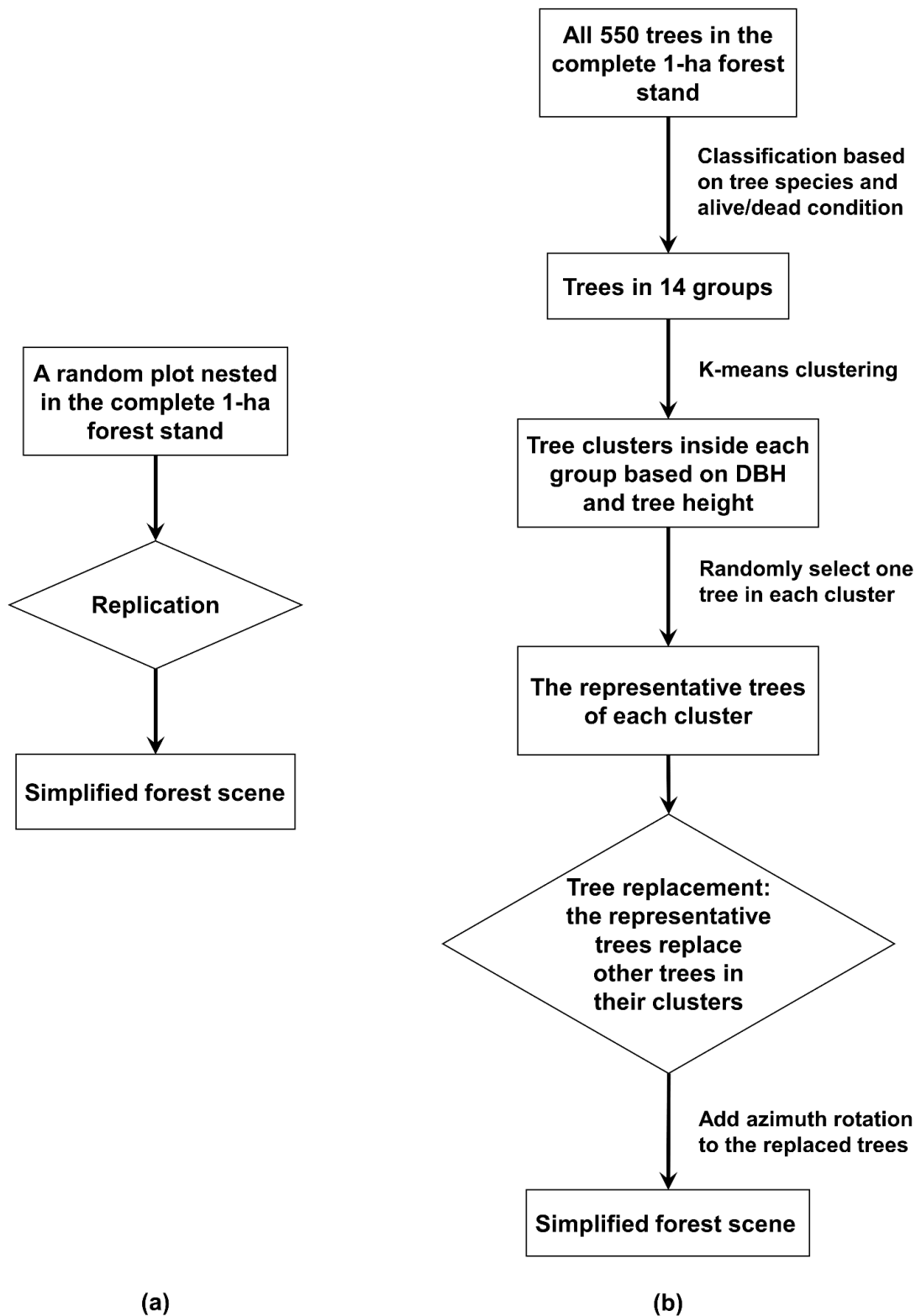
**Figure 2.** Conceptual diagram of the subsampling methods: (a) subplot method; (b) tree library method.

## 2.4.2 Tree library subsampling method (tree-based)

This method utilizes representative trees as subsets to represent the entire forest stand (Figure 2b). To sample the trees, we first classified all 550 trees into 14 groups according to the tree species and live/dead condition (seven tree species multiplied by two conditions) (Table 1). Then the DBH and height of each tree were normalized for each group. The relative tree height and DBH were then used as inputs in a K-means clustering algorithm to divide the tree individuals into several clusters. We sampled one tree in each cluster to reconstruct the simplified forest scene, so that the total number of trees sampled was equal to the number of clusters. Therefore, in each group, the number of clusters was equal to the number of trees in this group multiplied by a sampling fraction (Figure 3). The sampling fraction ranged between 10% and 90%, with an interval of 10%. For each clustering, the K-means algorithm (K-means function in MATLABR2022a) was repeated 20 times with different random initial centroids. The result with the lowest total sum of distances among all the replicates was used. After clustering (Figure 3), a random tree was selected in each cluster. The other trees in this cluster were replaced by this selected tree in the RT simulation.

To quantify the uncertainty of the tree library subsampling method, we reconstructed 100 simplified forest scenes for each sampling fraction. To do so, we repeated the above subsampling 100 times for each sampling fraction. The azimuth orientation is a commonly used step in subsampling of previous research to create more diverse forest scenarios (e.g., Widlowski et. al., 2014; Janoutová et. al., 2019). We varied the azimuth orientation of the replicated trees during the reconstruction. For the first 24 forest scenes, the replicated trees had an azimuth rotation of 15 x n degree (n= 0 to 23); for the 25th to 50th forest scenes, the replicated trees had a random azimuth rotation; for the 51st to 100th forest scenes, the processing was the same as the 1st to 50th scenes, except we randomly set whether the replicated trees were rotated or not. There were 900 simplified forest scenes reconstructed in total (9 sampling fractions x 100 forest scenes/fraction).
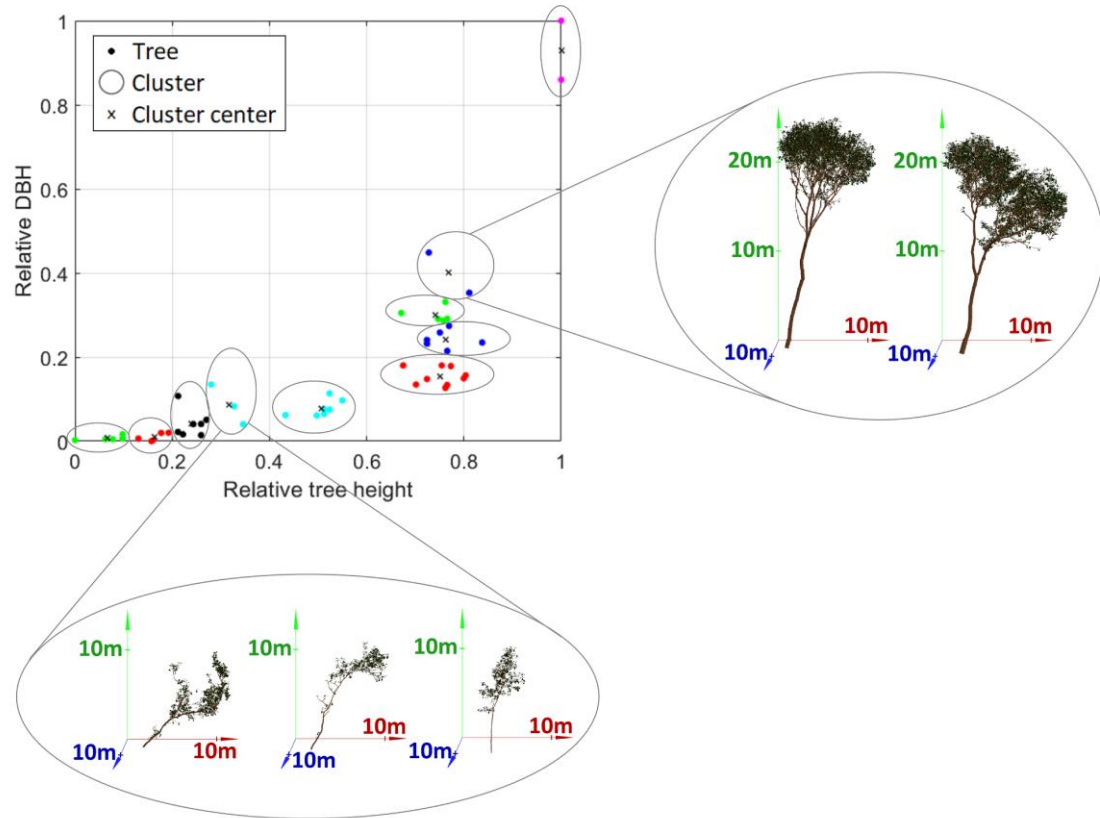
**Figure 3.** Illustration of tree clustering in each group: 50th clustering of living common ash with 20% sampling fraction (i.e., the 51 trees were clustered into 51 x 20% ≃ 10 clusters). The different colored dots represent trees in each cluster.

## 2.5 Radiative transfer modeling

We used the Discrete Anisotropic Radiative Transfer (DART) model (Gastellu-Etchegorry, 2008; Gastellu-Etchegorry et al., 2012, 2004, 1996) to conduct RT simulations in this study (DART 5.8.10, v1259). The DART model simulates the Earth-atmosphere radiation interactions from visible to thermal infrared wavelengths. It has been comprehensively benchmarked against other RTMs for simulating vegetation canopy reflectance (Widlowski et al., 2015).

We simulated the nadir orthorectified BRF images of the reconstructed forest scenes. In the simulation, we replicated the solar angle, and spatial and spectral resolutions during the UAV field data collection. At each waveband, the full width at half maximum of the UAV sensor was used as the bandwidth in the simulation. To ensure energy conservation, the scene was cloned around itself in the

RT simulation. We slightly shifted the altitude of DEM's edge during the replication to ensure the continuity of topography and scene (see "infinite slope" in Gastellu-Etchegorry, 2021; Wang et al., 2020).

## 2.6 Evaluation method

### 2.6.1 Benchmarking DART simulations using UAV imagery

We first benchmarked the assessed performance of DART simulations using the UAV dataset as the reference. The simulation accuracy was evaluated at both stand scale and pixel level.

At stand scale, the simulation accuracy was evaluated using the correlation coefficient (R). The simulated BRF of the complete 1-ha forest stand was compared with the UAV images. For each waveband, we calculated the mean BRF value ($BRF_{mean}$) of the images. The correlation coefficient between UAV $BRF_{mean}$ and DART simulated $BRF_{mean}$ were calculated at the spectral domain using equation (1).

$$R = \frac{\sum_{b=1}^{w}(UAV_b - \overline{UAV})(DART_b - \overline{DART})}{\sqrt{\sum_{b=1}^{w}(UAV_b - \overline{UAV})^2 \sum_{b=1}^{w}(DART_b - \overline{DART})^2}} \qquad 1)$$

where $UAV_b$ and $DART_b$ are the mean *BRF* of the UAV image and the DART image on waveband b, $\overline{UAV}$ and $\overline{DART}$ are the mean value of $UAV_b$ and $DART_b$ over all wavebands, and *w* is the total number of wavebands (32).

At pixel level, we compared the BRF of DART simulations and UAV dataset pixel by pixel. We used correlation coefficient to evaluate the simulation accuracy:

$$R = \frac{\sum_{i=1}^{n}(UAV_i - \overline{UAV})(DART_i - \overline{DART})}{\sqrt{\sum_{i=1}^{n}(UAV_i - \overline{UAV})^2 \sum_{i=1}^{n}(DART_i - \overline{DART})^2}} \qquad 2)$$

Where $UAV_i$ and $DART_i$ are the BRFs of pixel *i* in UAV image and DART image, on a certain band. $\overline{UAV}$ and $\overline{DART}$ are the mean BRF value of the UAV and DART images on this band. *n* is the total pixel number in an image. The evaluation was conducted at multiple spatial resolutions: 20 cm, 1 m, and 10 m, corresponding to the original UAV image, moderate-resolution UAV sensor or high-resolution satellite observation, and Sentinel-2 observation. For resolutions coarser than original UAV image (20 cm), the UAV and DART simulated images were down sampled by averaging neighbor

pixels. To eliminate the impact of border canopy on evaluation, only the central area of the 1-ha forest scene (i.e., 80 x 80 m²) was used for the pixel-level evaluation.

## 2.6.2 Quantifying the deviation of simplified forest scenes in radiative transfer modeling

After the benchmarking of the DART simulation, the RT simulation of the complete 1-ha forest scene was used as the reference. The normalized mean deviation ($\overline{ND_b}$) and normalized mean absolute deviation ($|\overline{ND_b}|$) of the simplified forest scenes were calculated to quantify their accuracy, as:

$$\overline{ND_b} = \frac{\sum_{s=1}^{p}(BRF_{sim,b}^{s} - BRF_{ref,b})}{p \times BRF_{ref,b}} \times 100 \qquad 3)$$

$$\overline{|ND_b|} = \frac{\sum_{s=1}^{p}|BRF_{sim,b}^{s} - BRF_{ref,b}|}{p \times BRF_{ref,b}} \times 100 \qquad 4)$$

where $BRF_{ref,b}$ was the $BRF_{mean}$ of the complete 1-ha forest scene at waveband $b$ and $BRF_{sim,b}^{s}$ is the $BRF_{mean}$ of the simplified forest scene $s$ at waveband $b$, and $p$ is the total number of simplified forest scenes built by subplot or tree library methods, given a specific sampling fraction. In this study, $p$ is 100.

Here we compared the RT simulations with one another, but not with UAV data. This ensured the subsampling of the forest stand was the only variable in the comparison and all the RT differences were caused by the subsampling of the forest stand.

# 3 Results and Discussion

## 3.1 Simulation benchmarking

The BRF simulations showed overall good agreement with UAV images at the forest stand scale (Figure 4) and also in fine detail (individual tree and twig level) (Figure 5, 6). For the mean BRF of the whole forest stand, the R between DART simulated and UAV imagery in the spectral domain was 0.99. DART simulations had larger ranges of pixel BRF than UAV images at all bands (Figure 4), which means there was a larger reflectance range between image pixels. The standard deviations of pixel BRFs in

each image were 0.051 vs. 0.076 for UAV images vs. BRF simulations, calculated from the average at all bands. For the two commonly used bands in vegetation monitoring (red and NIR), the BRF difference between DART simulated and UAV measured BRF was -0.002 and +0.0067 at the red and NIR bands, respectively which represents a relative deviation of -10.3% and +1.9% after normalizing by the UAV data. The standard deviations of UAV measured vs. DART simulated pixel BRFs were 0.0086 vs. 0.012 and 0.13 vs. 0.18 for red and NIR bands, respectively.

The DART simulations and UAV images also showed good similarity in fine detail. The canopy shapes and the structure of stems and branches in the DART simulated images showed high similarity to the real forest (Figure 5). The pixel level evaluation showed good correlation (Figure 6). In the NIR band, the R between UAV and DART simulated pixels BRF increased from 0.6 to 0.92, as the spatial resolution varied from 0.2 m to 10 m. While in the red band, the R was lower than the NIR band, it increased from 0.45 to 0.67 under same resolution change. The motion of the UAV sensor is one reason causing the differences between simulated and UAV data; the UAV images were taken from a moving platform, and the final images were thus subject to some level of motion blur. Furthermore, the image pixels of size of 20 cm were calculated by averaging two by two 10 cm initial image pixels, and averaging was also used to produce other pixel sizes. This averaging caused UAV images to have fewer BRF differences among pixels. Therefore, UAV images were more blurred than DART simulated images, causing the pixel level difference between them. Another factor causing differences between the simulated and UAV data is that the UAV orthomosaic was composed from the central perspective with images having view zenith angles of 0-6 degrees and on average 3 degrees. The resulting reflectance anisotropy effects were considered insignificant in this study. Besides, the imperfections of geolocation registration and in-situ measured spectral properties could also cause the differences between UAV and DART simulated images, especially at pixel level.

Our results are comparable with corresponding studies in the literature. Janoutová et al. (2019) compared DART simulations of Norway spruce 3D scenes (10 x 10 m$^2$) with airborne hyperspectral CASI–SASI images and satellite Sentinel-2 MSI images. The RMSEs of mean reflectance were between 0.02-0.05. Schneider et al. (2014) compared the modeled mean at-sensor radiances to the at-sensor radiances measured by the Airborne Prism Experiment imaging spectrometer. The mean relative difference is 36.4% in the visible spectral range.

In summary, the results showed BRF simulations had relatively good similarities with the UAV

measured data. Thus the RT simulations of this complete 1-ha forest scene were capable of reproducing the structure and reflectance of the real forest stand and were qualified to be used as the reference data for the following experiments.
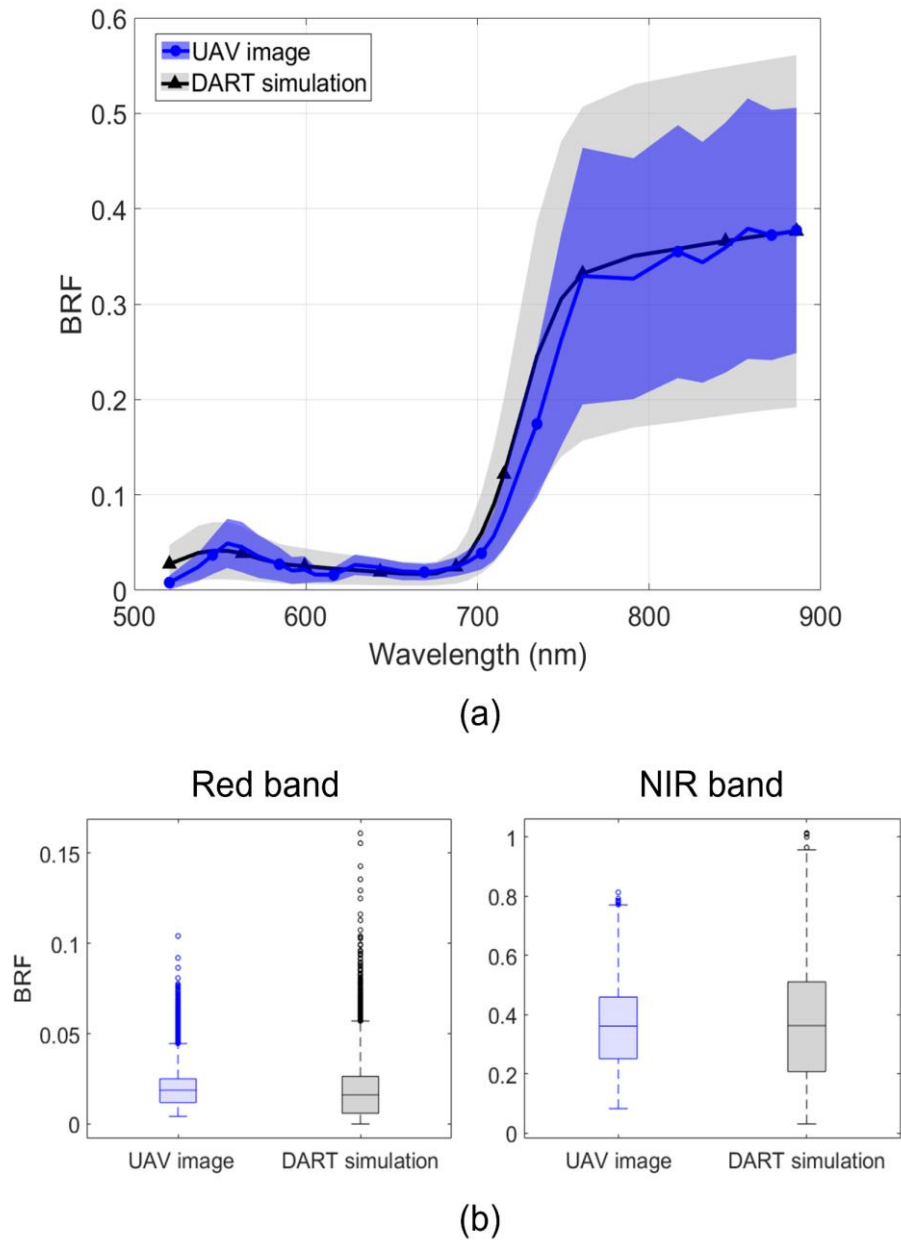


(a)

(b)

**Figure 4.** Comparison between UAV measured and DART simulated forest Bidirectional Reflectance Factors (BRF). (a) Mean BRF value in the spectral domain. The shaded area is the standard deviation of pixel BRF in each band's image. (b) Boxplot of pixel BRF at red and NIR bands.
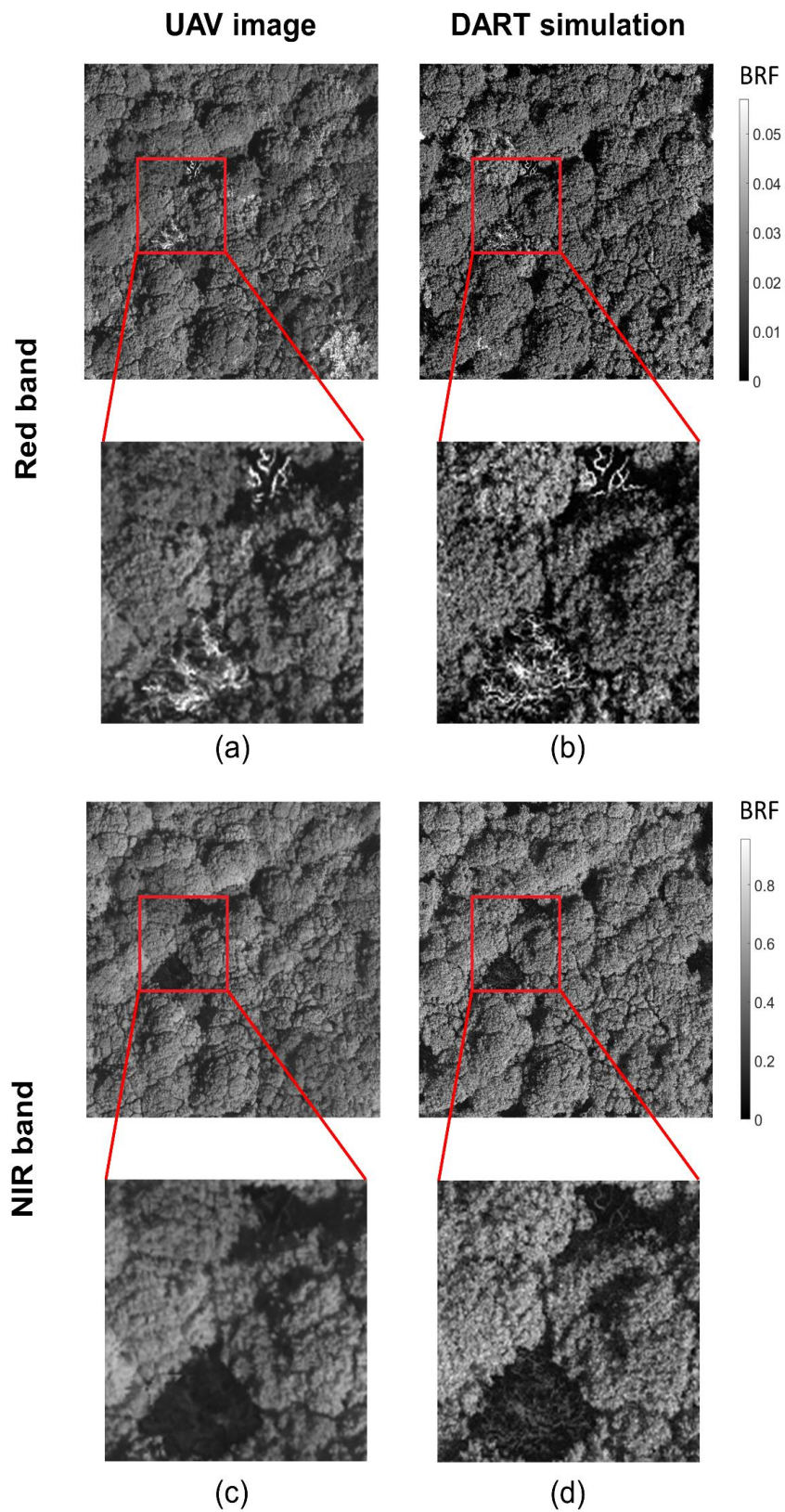
**Figure 5.** Comparison between UAV measured and DART simulated forest nadir images. (a)(b) UAV and DART simulated images at the red band. (c)(d) UAV and DART simulated images at the NIR band.

**Red band**

**NIR band**

**0.2 m**

R = 0.45

R = 0.60

**Spatial resolution**

**1 m**

R = 0.69

R = 0.80

**10 m**

R = 0.67

R = 0.92

(a)

(b)

(c)

(d)

(e)

(f)
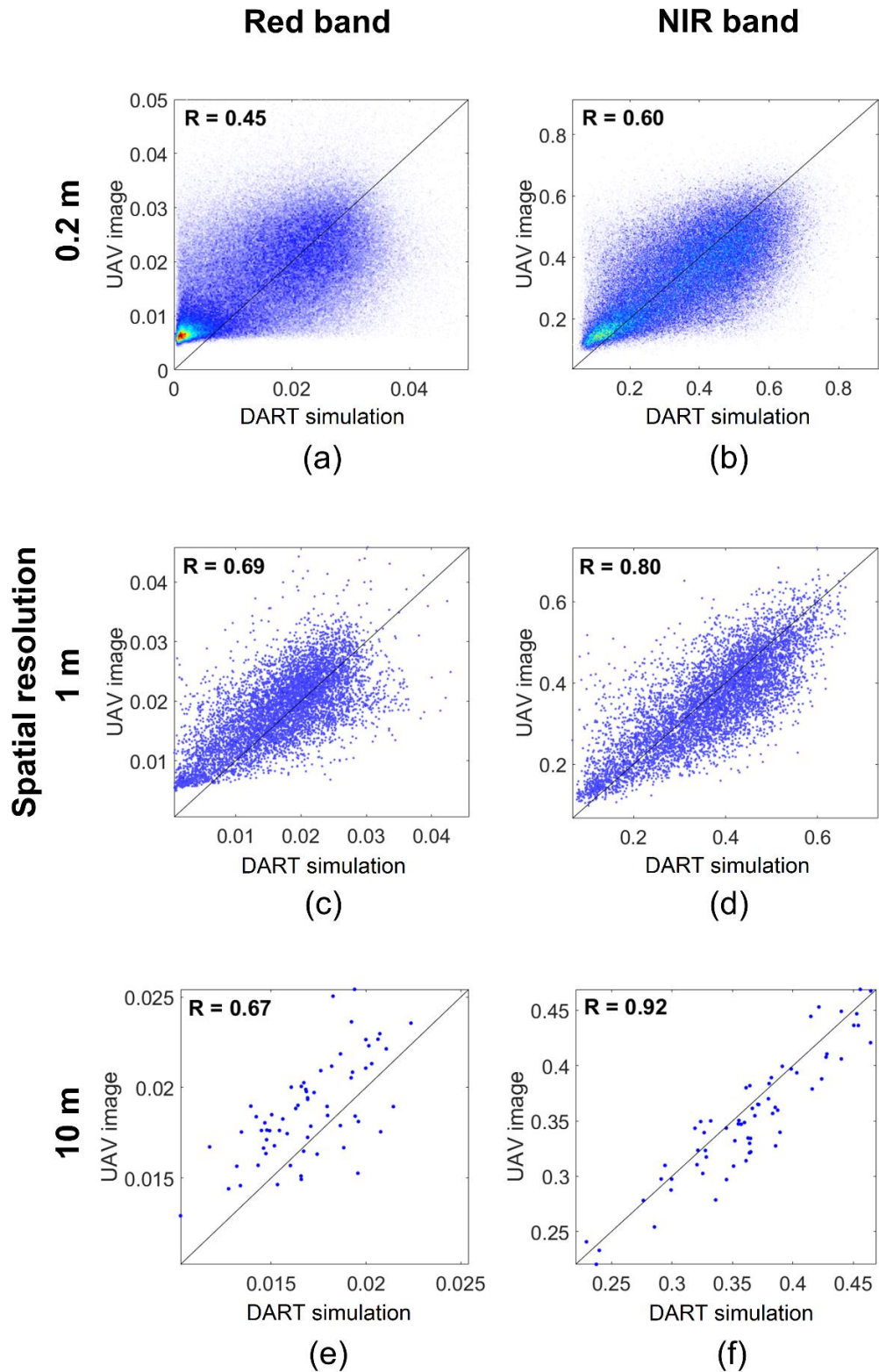
**Figure 6.** Pixel by pixel scatter plot between UAV measured and DART simulated Bidirectional

Reflectance Factors (BRF). The black solid line represents the 1:1 line.

## 3.2 Impact of sampling fraction on reflectance deviation

On average, the deviation and uncertainty of the subplot and tree library subsampling method decreased as the sampling fraction increased. As the sampling fraction increased from 10% to 90%, the normalized mean BRF deviation of the subplot method decreased from -2.7% to -0.0034% and its standard deviation decreased from 7.7% to 0.54% (Figure 7a, Figure A3). The absolute deviation decreased from 6.7% to 0.47%. The corresponding standard deviation decreased from 4.7% to 0.28% (Figure A5a).

Meanwhile, for the tree library method, the normalized mean BRF deviation decreased from -7.4% to -1.3% and its standard deviation decreased from 2.8% to 0.51% (Figure 7b, Figure A4). As for the absolute deviation, it decreased from 7.4% to 1.3%. And the corresponding standard deviation decreased from 2.7% to 0.51% (Figure A5b). Accordingly, appropriate sampling fractions should be used depending on the accuracy requirements of different RS applications (e.g, one-time observation or dynamic monitoring).

The normalized BRF deviation of the simplified forest scenes was lowest at the red band (669 ± 13.25 nm) for all sampling fractions (Figure 7ab, Figure A3, A4). Although subsampling caused more canopy gaps (74.2% scenes had smaller canopy cover than complete 1-ha scene)and shadows in the image in total, it also allowed more light to pass through the canopy and reach the ground. While at the red band, the reflectance difference between understorey and leaf (of the three dominant tree species) was the largest among all bands: 0.075 vs. 0.045, 1.7 times. This higher light reflection of the understorey, together with more light reaching the ground due to the increased canopy gap, caused more light to be reflected from the ground to the sensor compared with other bands. This compensated for the lower reflectance caused by more shadows, resulting in the lowest normalized BRF deviation.
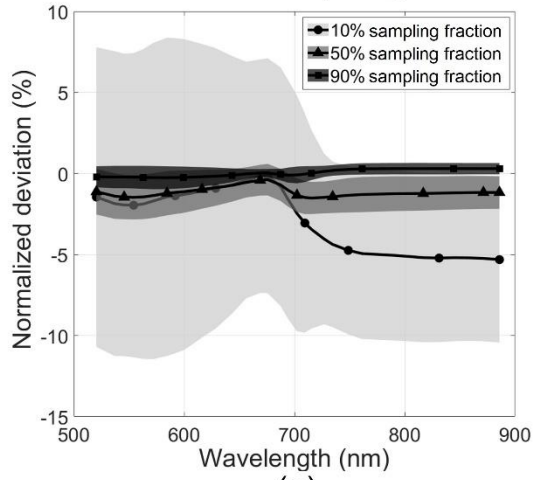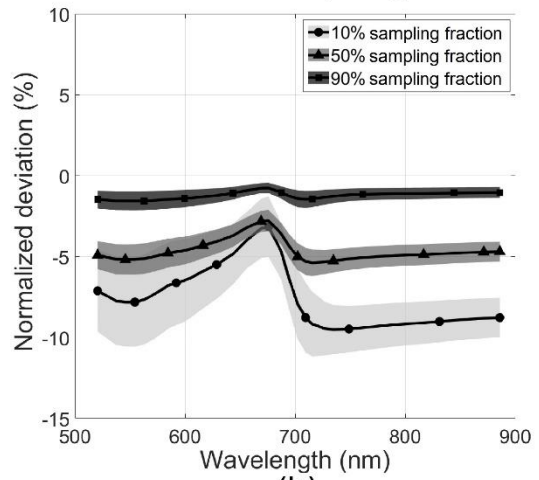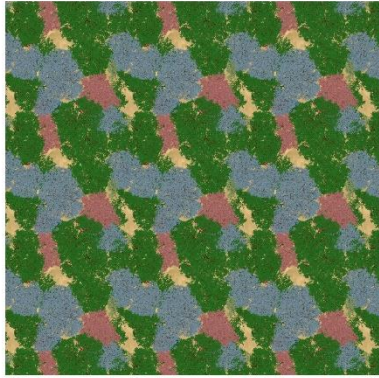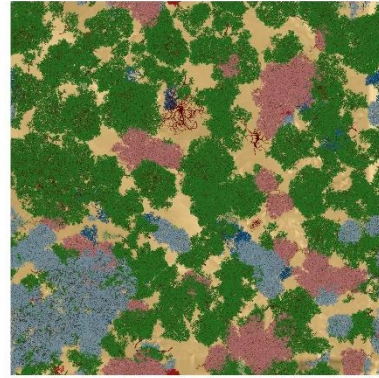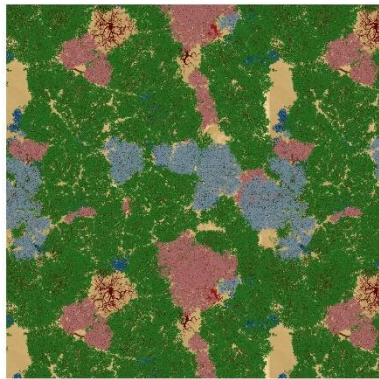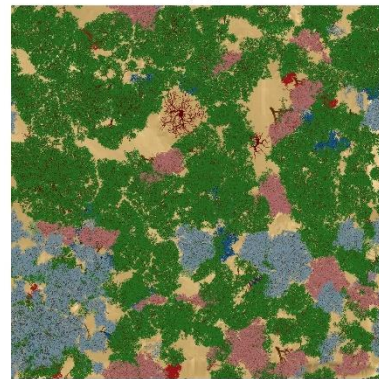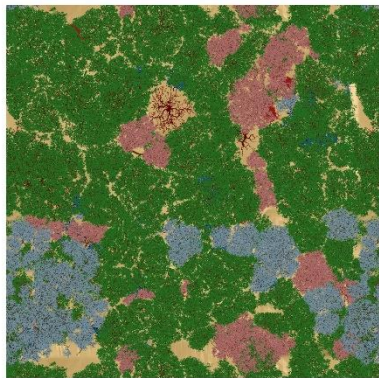
**Figure 7.** The normalized BRF deviations of simplified forest scenes built from the subplot and the tree library subsampling methods. And the top view of some corresponding simplified forest scenes. (a-b) The normalized BRF deviations of the subplot and the tree library subsampling methods. The shaded area is the standard deviation. (c-h) One of the 100 reconstructed simplified forest scenes for each subsampling method and sampling fraction. The different leaf colors represent the different tree species.

Côté et al. (2012) investigated the impact of the tree library subsampling method on plot-level forest structure (DBH, leaf area, basal area, and vertical distribution of canopy elements). They selected five trees representing four tree species to reconstruct the simplified forest scene (0.4-hectare plot including 279 individual trees).  However, the impact of subsampling on the radiative transfer (e.g., reflectance) was not investigated. Other research (Côté et al., 2009; Janoutová et al., 2019; Widlowski et al., 2015, 2014) used the subsampling method as a strategy to generate 3D forest scenes and did not investigate the impact of the subsampling method on the realism of forest structure and radiative transfer. Here we found that for simulating forest reflectance, preserving realistic forest structural and spectral properties play an important role in the realism of reconstructing forest scenes. Normalized BRF deviation values of subsampling have a high correlation with these forest properties (Table 2). Some forest properties have a significant impact on the BRF deviation, depending on the wavelength. For example, in the NIR band, the correlation coefficient (R value) between BRF deviation and canopy cover was 0.88, with LAI was 0.36; in the green band, the R-value between BRF deviation and leaf reflectance was 0.58, and with canopy cover this value was 0.53; and in the red band, mean DBH (R 0.39) and tree density (R 0.37) were more impactive on BRF deviation than other properties.

Table 2. Correlation coefficient (R) between forest structural/spectral properties and normalized BRF deviations caused by subsampling in three wavelength bands. The last row shows the R-value between normalized BRF deviations and all the above properties together. The R-value was calculated from linear fit with intercept.

| | Green | Red | NIR |
|---|---|---|---|
| **Canopy cover** | 0.53 | 0.25 | 0.88 |
| **LAI** | 0.13 | -0.19 | 0.36 |
| **Tree density** | -0.13 | -0.37 | 0.04 |
| **Mean tree height** | -0.02 | 0.14 | 0.22 |
| **Mean DBH** | 0.21 | 0.39 | 0.23 |
| **Mean leaf reflectance weighted by LAI** | 0.58 | 0.06 | 0.08 |
| **WAI** | -0.07 | -0.15 | 0.22 |
| **All** | **0.88** | **0.6** | **0.92** |

## 3.3 Comparison between different subsampling methods

For subsampling fractions 20% to 90%, the normalized mean (and absolute) BRF deviations of the subplot method were smaller than the tree library method (Figure 8, Figure A6). Although the uncertainty of the subplot method was higher than the tree library method, the upper limits of the subplot method's deviation were still lower than that of the tree library method. Here the upper limit of deviation was the largest deviation considering the subsampling uncertainty and was calculated as the normalized mean absolute deviation plus its standard deviation (the upper border lines of the shaded area in Figure A6).

The subplot method performs worse than the tree library method in visible bands with a small number of samples (Figure A6, 10% fraction): the mean absolute deviation and standard deviation are both higher. With the 10% sampling fraction, the subplot methods have higher upper limits of deviation at the green, red, and all 32 bands from 520 to 886 nm  (normalized absolute deviation plus standard

deviation was around 11.6%); while at the NIR band, the upper limits of deviation of tree library method's accuracy were equal to subplot method (10.2%) (Figure A6). Although the subplot sampling method is more accurate than the tree library method on average, its larger uncertainty might lead to higher deviation for some simplified forest scenes when the subsample size is too small. With the 10% sampling fraction and on the red band, simplified forest scenes built from the subplot method were more likely to have a normalized BRF deviation larger than 5% compared to the tree library method: probability 34% vs. 13%; and under the 10% sampling fraction and green band, simplified forest scenes built from subplot method were more likely to have a normalized deviation larger than 10% compared to the tree library method: probability 31% vs. 22%. But if the sampling fraction was larger than 10%, the subplot method was more accurate than the tree library method (Figure 8, Figure A6).

As discussed in section 3.2, unrealistic canopy cover was one of the major reasons for the reflectance deviation of subsampling methods in this closed-canopy forest. For the subplot method, this deviation occurred only at the boundary of the subplot. While for the tree library method, this deviation occurred for every individual tree border. Therefore, there were more canopy gaps in the scene constructed by the tree library method (Figure 7cd) compared to the real forest, which caused less accurate results. Meanwhile, the tree library method ensured the same tree density in all reconstructed forest scenes (550 trees/ha). Thus its uncertainty was smaller than the subplot method. If the application had a relatively more flexible accuracy requirement (e.g., maximum 15% normalized deviation), and wanted to use very limited data (e.g., 10% sampling fraction) to represent a large-scale site, then the subplot method would perform slightly worse than the tree library method (Figure 8, Figure A6 data at 10% sampling faction). Under these conditions, the probability of the subplot method meeting this requirement was 96%, compared to 100% for the tree library method. But considering the overall performance under all and sampling fractions (Figure 8, Figure A6), the subplot method is sufficiently superior to the tree library method.
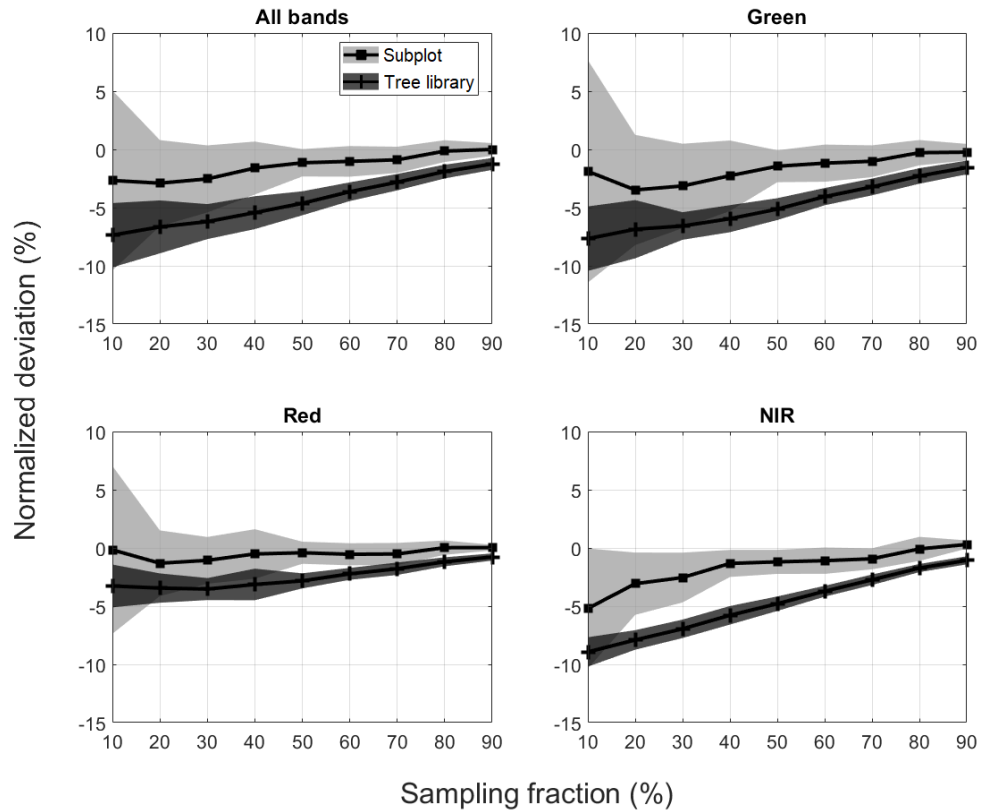
**Figure 8.** Comparison between subplot and tree library subsampling methods' normalized BRF deviations. The different subfigures show the results for all, green, red, and NIR bands, respectively. Solid lines are the mean values. The shaded areas are the standard deviations.

## 3.4 Optimal subsampling strategies

With more samples used to reconstruct the forest scene, the deviation of the tree library method substantially decreased: absolute normalized deviation decreased from 7.4% to 1.3%. The deviation decrease amount of the tree library method was relatively unchanged while more trees were used in the reconstruction. For each additional 10% of trees used, the reduction of absolute normalized deviation ranged between 0.45% and 0.99% (Figure 9b). While the deviation decrease of the subplot method was less noticeable (from 2.7% to 0.0034%) than the tree library method and occurred mainly when the sampling plot area increased from 30% to 40% (decreased by 0.93%) or 70% to 80% (decreased by 0.75%) (Figure 9a).

The uncertainty of the subplot method remarkably decreased as more samples were used to reconstruct the forest scene (standard deviation reduction from 7.7% to 0.54%). The reduced uncertainty of the subplot method occurred mainly when the sampling plot area increased from 10% to 20%: the

standard deviation decreased by 4% (Figure 10a). This decrease was larger than the total decrease in other sampling fractions (from 20% to 90%), which was 3.16%. Meanwhile, the uncertainty decrease of the tree library method was less obvious (from 2.8% to 0.51%) than the subplot method and occurred mainly when the sampling tree number increased from 10% to 30% (decreased by 1.26%) (Figure 10b).

Sampling 20% of the forest area and using the subplot method to build the forest scene is an effective reconstruction strategy for this closed-canopy temperate deciduous forest. This strategy ensured a mean normalized BRF deviation of -2.90% and a standard deviation of 3.70% in the forest stand studied, with a relatively low reconstruction effort. If the typical uncertainty associated with vicarious calibration efforts of satellite observations (Bruegge et al., 2002; Kneubuhler et al., 2002; Thome, 2001; Thome et al., 2008; Wang et al., 2011), which is 5%, was used as the deviation tolerance criterion, the normalized BRF deviations of 66.4% reconstructed forest scenes can meet this criterion using the above subsampling strategy at all 32 bands from 520 to 886 nm. This probability was 99% and 100% for the criteria of less than 10% and 15% deviation, respectively.
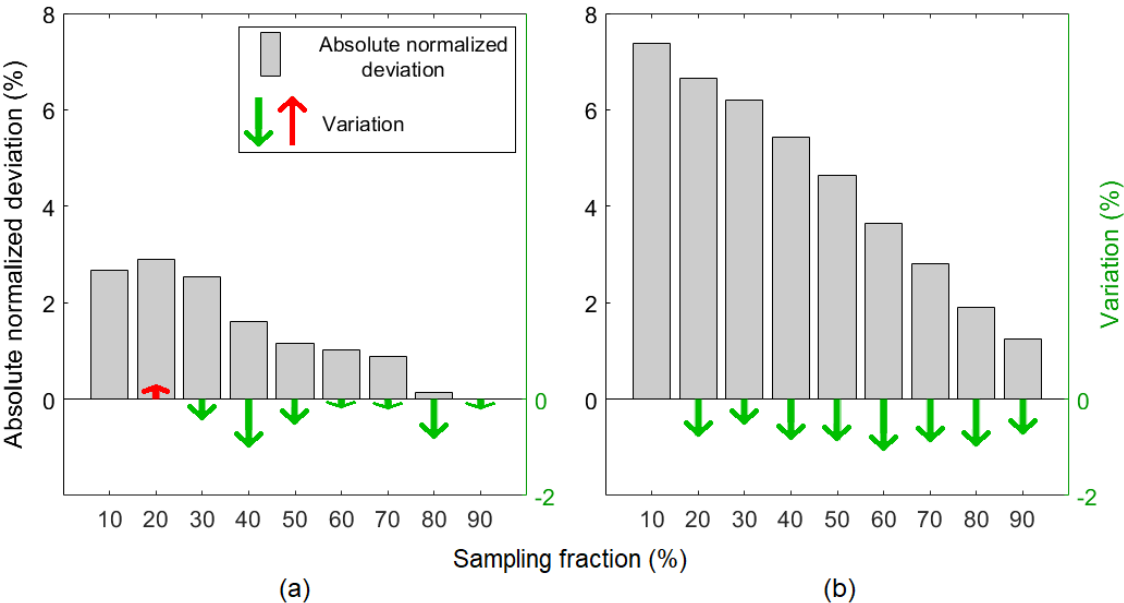


**Figure 9.** Accuracy improvement caused by each 10% increase in sampling fraction. (a) subplot subsampling method. (b) Tree library subsampling method. The green and red arrows show the change in absolute normalized deviation for each 10% increase in sampling fraction. The grey bar is the absolute normalized deviation value under a certain sampling fraction.
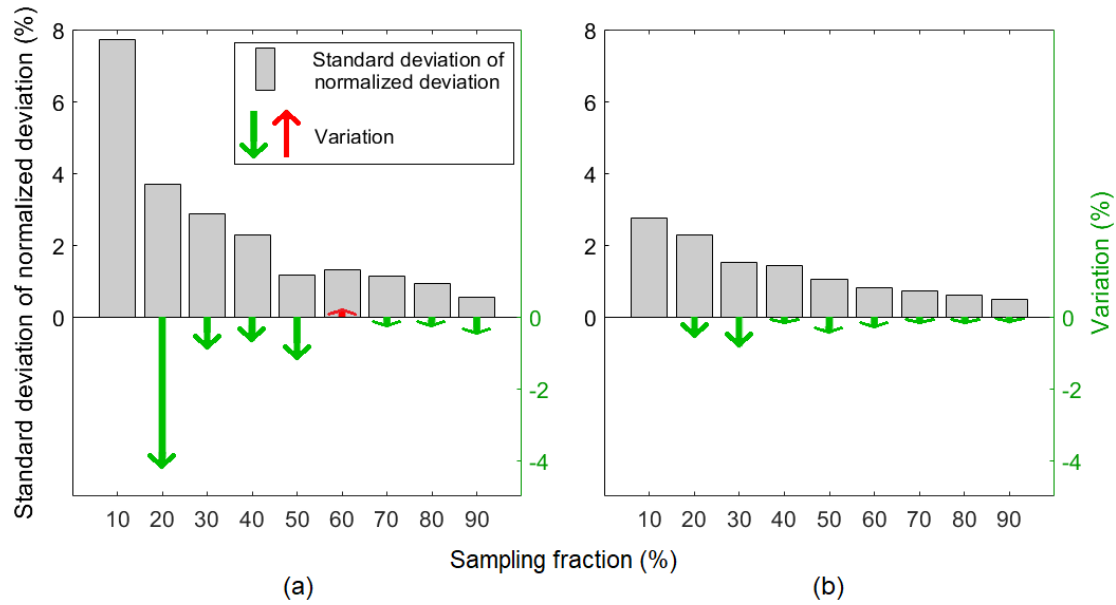
**Figure 10.** Uncertainty reduction caused by each 10% increase in sampling fraction. (a) subplot subsampling method. (b) Tree library subsampling method. The green and red arrows show the change in the standard deviation of normalized BRF deviation for each 10% increase in sampling fraction. The grey bar is the standard deviation value under a certain sampling fraction.

Based on RT simulations of 1800 different forest scenes built by subsampling methods, we found that depending on the waveband, the canopy cover, LAI, leaf reflectance, tree density, and DBH have a relatively large impact on the nadir reflectance deviation for the closed-canopy temperate deciduous forest when using forest subsampling methods to upscale the forest scene (Table 2). These properties should be used as the quality index when applying subsampling methods to closed-canopy temperate deciduous forest scenes.

For the reconstruction of forests at a large scale, we suggest first using high-resolution satellite imagery to quantify the heterogeneity of the forest. Then dividing the forest into forest stands with similar structural/spectral attributes, and physiognomy, mainly on canopy cover, LAI, leaf reflectance, and tree density. For each forest stand, an appropriate subplot scale that can capture the variability of this forest stand should be determined. For example, the subplot of 20% stand area is a such scale in this study. The subsampling method can be used with this subplot scale to reconstruct large-scale 3D-explicit forest scenes for RT modeling, using the above structural and spectral properties as the quality index.

Our research was based on a typical closed-canopy temperate deciduous forest. For other forest

types with different canopy cover (e.g., savannas) or understorey reflectance (e.g., variable reflectance due to rain, seasonal fallen leaves, or bush), further research is needed.

# 4 Conclusion

This study quantified the reflectance differences resulting from two main subsampling methods of varying sampling fractions for a typical closed-canopy temperate deciduous forest. RT modeling of a 1-ha 3D-explicit forest scene was used to simulate canopy BRF and evaluate method trade-offs. The results showed that sampling 20% of the forest area using the subplot subsampling method was an effective reconstruction strategy for the closed-canopy temperate deciduous forests similar to this site. Furthermore, from the RT modeling perspective, preserving realistic canopy cover, LAI, leaf reflectance, tree density, and DBH  is important for achieving reconstruction realism.

This study provides guidance for the 3D-explicit reconstruction of temperate deciduous forest scenes (with cm-level accuracy) at the forest stand scale (≥ 1-ha). Accordingly, highly realistic EO data can be modeled at the forest stand scale to aid with numerous possible RS applications (e.g., retrieval algorithm development, sensor design, understanding forest RT processes, or RS calibration and validation activities). Such realistic RT modeling of real forest stands can provide sufficient data for training artificial intelligence for RS interpretation or understanding forest RT processes. 3D-explicit forest scenes also allow modeling RS imagery at the cm-level resolution, which could support future ultra-high resolution satellite sensor designs, as well as the development of new RS products from high-resolution RS data to aid climate change, carbon cycle, forest dynamic monitoring, or other research.

This study was based on a typical closed-canopy temperate deciduous forest. Future studies are needed on a range of forest types to allow for an in-depth understanding of the impact of forest subsampling on RTMs.

# Acknowledgements

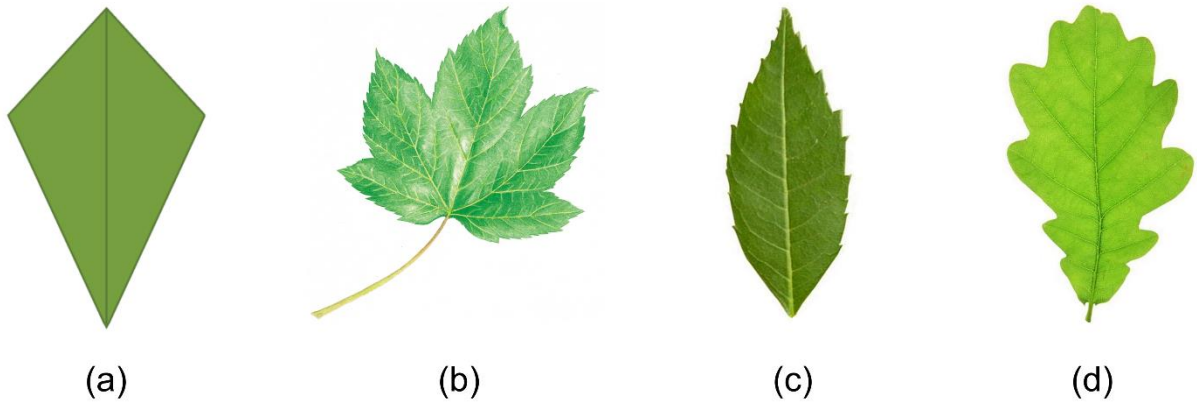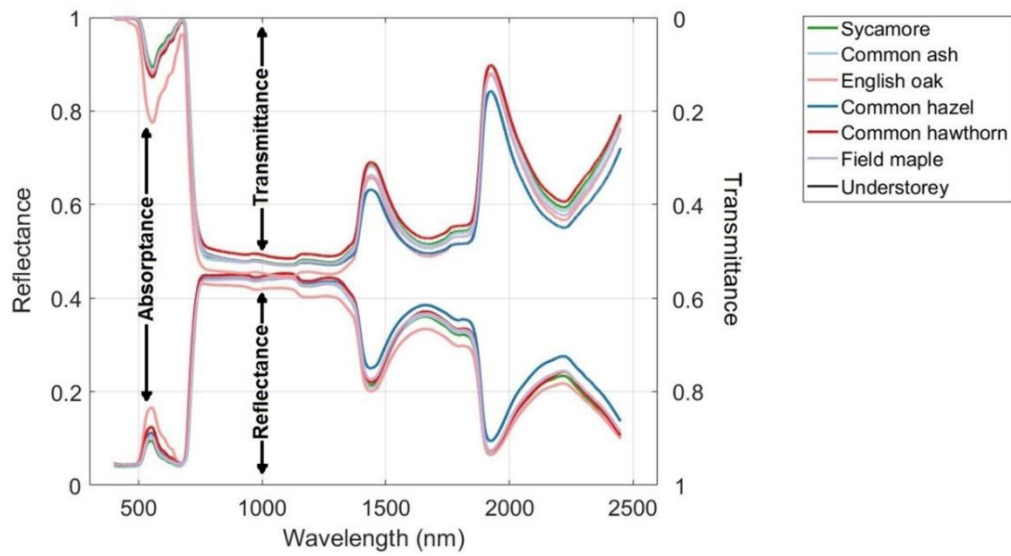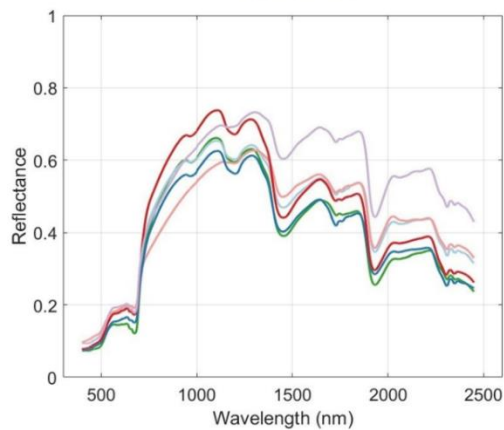# Appendix A



| (a) | (b) | (c) | (d) |

**Figure A1.** Reconstructed leaf shape compared with real leaves of dominant tree species in the study site: (a) reconstructed leaf; (b) Sycamore leaf; (c) Common ash leaf (single petal of a leaf); (d) English oak leaf.
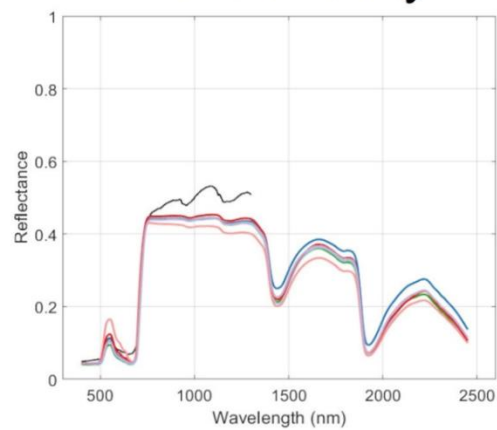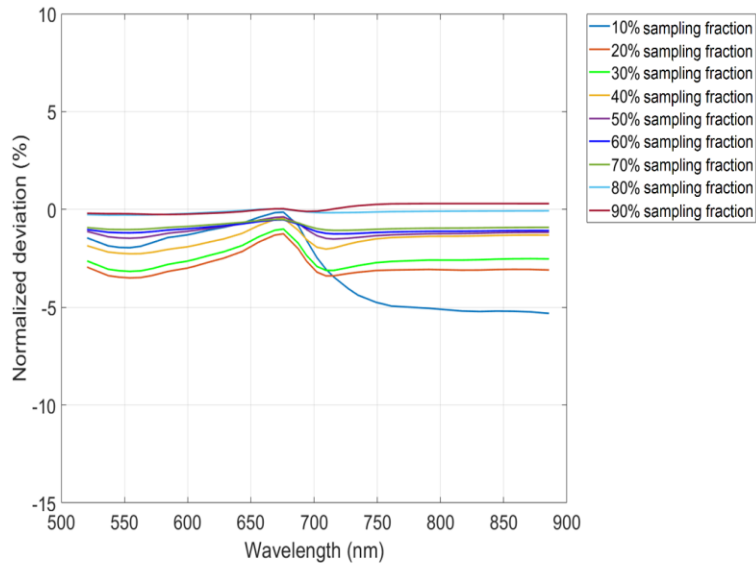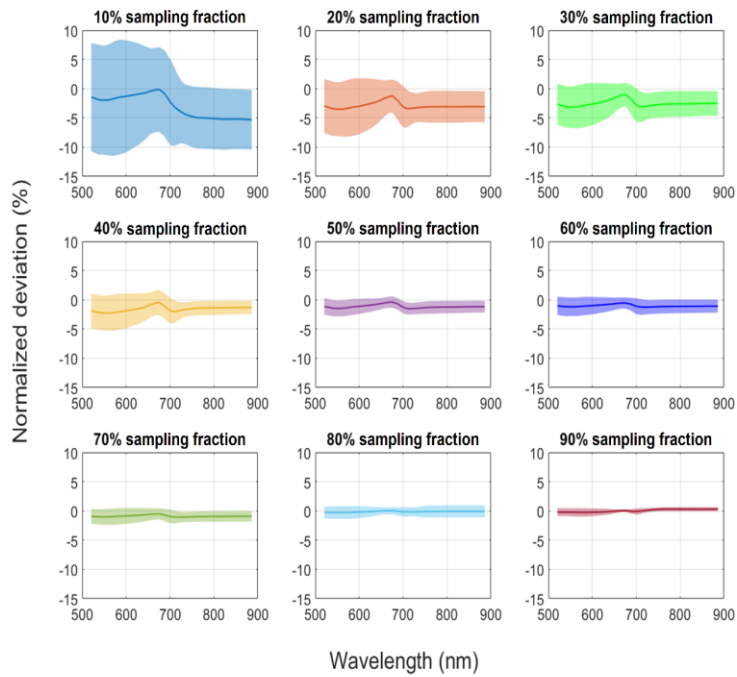
**Figure A2.** Spectral properties of different tree species. (a): Reflectance and transmittance of leaves. (b): Reflectance of bark. (c): Reflectance of understorey (black), together with reflectance of leaves as a comparison.
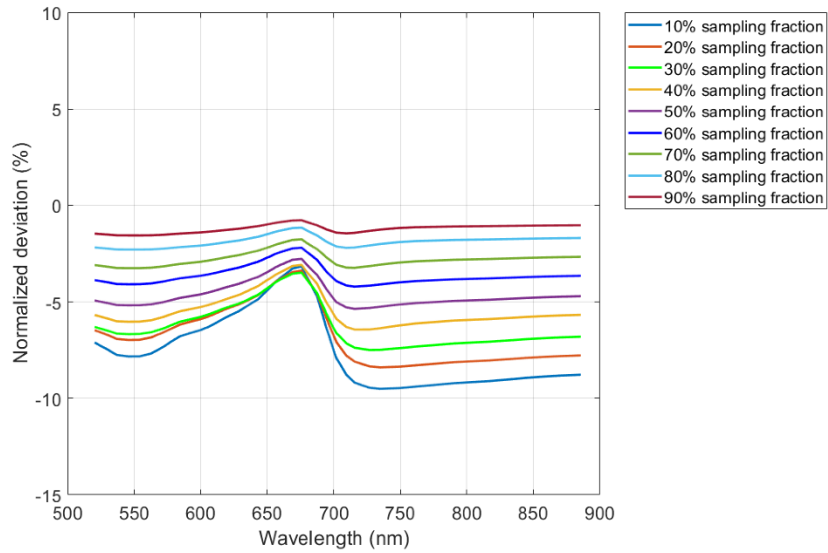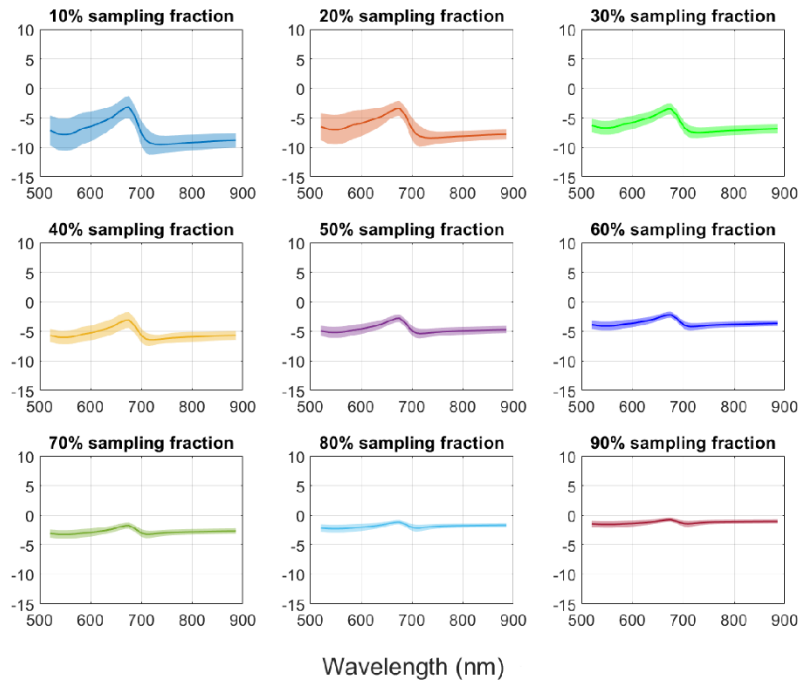
(a)



(b)

**Figure A3.** The mean and standard deviation of the subplot subsampling method's normalized BRF

deviation at all 9 sampling fractions (10% - 90% with a step of 10%). (a) Mean value; (b) Standard

deviation (shaded area).

(a)



(b)

**Figure A4.** The mean and standard deviation of the tree library subsampling method's normalized BRF deviation at all 9 sampling fractions (10% - 90% with a step of 10%). (a) Mean value; (b) Standard deviation (shaded area).

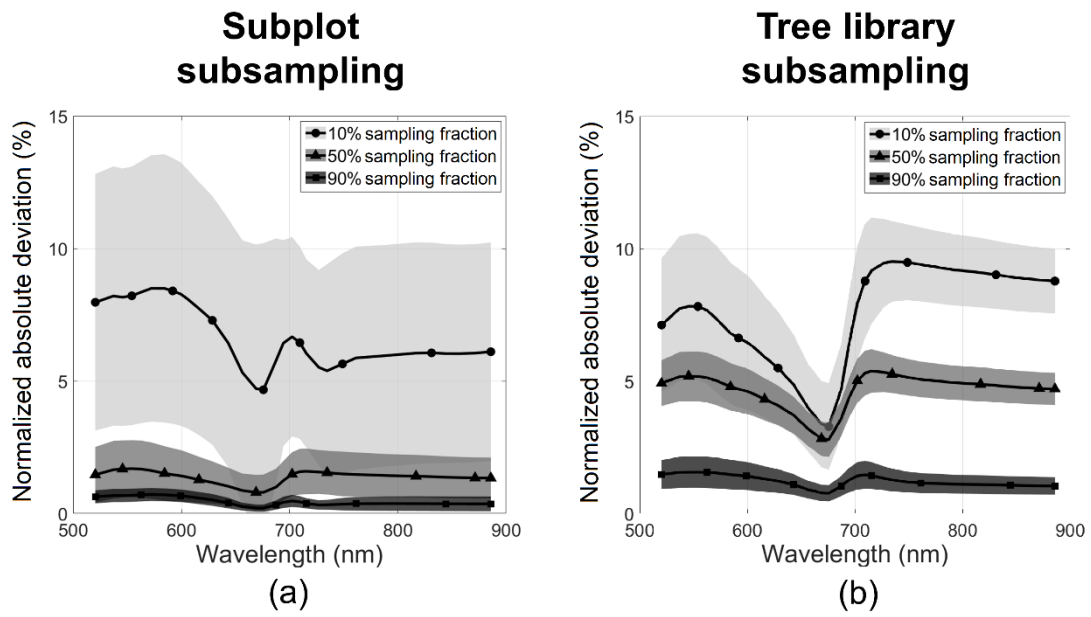**Subplot subsampling**

**Tree library subsampling**

**Figure A5.** The normalized absolute BRF deviations of simplified forest scenes built from the subplot and the tree library subsampling methods. The shaded areas are the standard deviations.
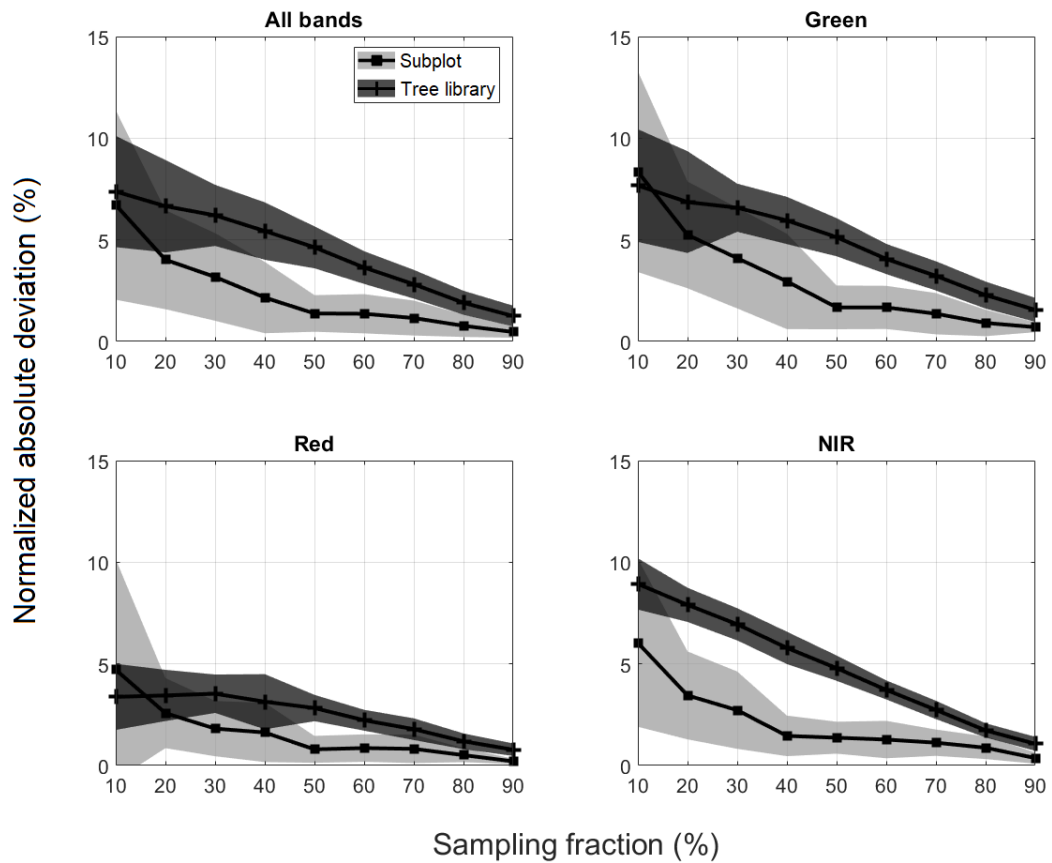
**Figure A6.** Comparison between subplot and tree library subsampling methods' normalized absolute BRF deviations. The different subfigures show the results for all, green, red, and NIR bands, respectively. Solid lines are the mean values. The shaded areas are the standard deviations.

**Table A1**. Waveband information of UAV dataset and radiative transfer modeling.

| Waveband | Central wavelength (nm) | Bandwidth (nm) | Waveband | Central wavelength (nm) | Bandwidth (nm) |
|---|---|---|---|---|---|
| 1 | 520.4 | 19.5 | 17 | 687.4 | 28.5 |
| 2 | 537.2 | 18 | 18 | 694.2 | 27 |
| 3 | 545.6 | 17.5 | 19 | 702.3 | 24 |
| 4 | 554.2 | 20.5 | 20 | 709.4 | 23.5 |
| 5 (Green) | 562.8 | 19 | 21 | 715.4 | 24.5 |
| 6 | 572.3 | 21.5 | 22 | 726.9 | 30 |
| 7 | 584.4 | 14 | 23 | 734.6 | 30 |
| 8 | 591.9 | 15.5 | 24 | 748.8 | 26 |
| 9 | 599.2 | 19.82 | 25 | 761.2 | 28.5 |
| 10 | 605.4 | 27 | 26 | 790.9 | 24.5 |
| 11 | 616.2 | 25.5 | 27 | 816.7 | 28 |
| 12 | 628.6 | 28.5 | 28 | 831.1 | 27 |
| 13 | 643.2 | 25.5 | 29 (NIR) | 844.5 | 27.5 |
| 14 | 656.3 | 27 | 30 | 857.5 | 29 |
| 15 (Red) | 669 | 26.5 | 31 | 871.3 | 30.5 |
| 16 | 675.7 | 26.5 | 32 | 885.9 | 27.5 |

# Reference

Åkerblom, M., Kaitaniemi, P., 2021. Terrestrial laser scanning: A new standard of forest measuring and modelling? Ann Bot 128. https://doi.org/10.1093/aob/mcab111

Bojinski, S., Verstraete, M., Peterson, T.C., Richter, C., Simmons, A., Zemp, M., 2014. The concept of essential climate variables in support of climate research, applications, and policy. Bull Am Meteorol Soc 95. https://doi.org/10.1175/BAMS-D-13-00047.1

Bruegge, C.J., Chrien, N.L., Ando, R.R., Diner, D.J., Abdou, W.A., Helmlinger, M.C., Pilorz, S.H., Thome, K.J., 2002. Early validation of the Multi-angle Imaging SpectroRadiometer (MISR) radiometric scale. IEEE Transactions on Geoscience and Remote Sensing 40. https://doi.org/10.1109/TGRS.2002.801583

Butt, N., Campbell, G., Malhi, Y., Morecroft, M., Fenn, K., Thomas, M., 2009. Initial Results from Establishment of a Long-term Broadleaf Monitoring Plot at Wytham Woods, Oxford, UK. Rep.

Calders, K., Adams, J., Armston, J., Bartholomeus, H., Bauwens, S., Bentley, L.P., Chave, J., Danson, F.M., Demol, M., Disney, M., Gaulton, R., Krishna Moorthy, S.M., Levick, S.R., Saarinen, N., Schaaf, C., Stovall, A., Terryn, L., Wilkes, P., Verbeeck, H., 2020a. Terrestrial laser scanning in forest ecology: Expanding the horizon. Remote Sens Environ. https://doi.org/10.1016/j.rse.2020.112102

Calders, K., Newnham, G., Burt, A., Murphy, S., Raumonen, P., Herold, M., Culvenor, D., Avitabile, V., Disney, M., Armston, J., Kaasalainen, M., 2015. Nondestructive estimates of above-ground biomass using terrestrial laser scanning. Methods Ecol Evol 6. https://doi.org/10.1111/2041-210X.12301

Calders, K., Origo, N., Burt, A., Disney, M., Nightingale, J., Raumonen, P., Åkerblom, M., Malhi, Y., Lewis, P., 2018. Realistic forest stand reconstruction from terrestrial LiDAR for radiative transfer modelling. Remote Sens (Basel) 10. https://doi.org/10.3390/rs10060933

Calders, K., Phinn, S., Ferrari, R., Leon, J., Armston, J., Asner, G.P., Disney, M., 2020b. 3D Imaging Insights into Forests and Coral Reefs. Trends Ecol Evol. https://doi.org/10.1016/j.tree.2019.10.004

Calders K., Verbeeck H., Burt A., Origo N., Nightingale J., Malhi Y., Wilkes P., Raumonen P., Bunce R. G.H., Disney M., 2022. Laser scanning reveals potential underestimation of biomass carbon in

temperate forest. Ecological Solutions and Evidence 3, e12197.

https://doi.org/https://doi.org/10.1002/2688-8319.12197

Côté, J.F., Fournier, R.A., Frazer, G.W., Olaf Niemann, K., 2012. A fine-scale architectural model of trees to enhance LiDAR-derived measurements of forest canopy structure. Agric For Meteorol 166–167. https://doi.org/10.1016/j.agrformet.2012.06.007

Côté, J.F., Fournier, R.A., Luther, J.E., van Lier, O.R., 2018. Fine-scale three-dimensional modeling of boreal forest plots to improve forest characterization with remote sensing. Remote Sens Environ 219. https://doi.org/10.1016/j.rse.2018.09.026

Côté, J.F., Widlowski, J.L., Fournier, R.A., Verstraete, M.M., 2009. The structural and radiative consistency of three-dimensional tree reconstructions from terrestrial lidar. Remote Sens Environ 113. https://doi.org/10.1016/j.rse.2009.01.017

Disney, M., 2019. Terrestrial LiDAR: a three-dimensional revolution in how we look at trees. New Phytologist. https://doi.org/10.1111/nph.15517

Gastellu-Etchegorry, J.P., 2021. DART User's Manual (5.7.9) [WWW Document]. URL https://dart.omp.eu/Public/documentation/contenu/documentation/DART_User_Manual.pdf (accessed 5.11.21).

Gastellu-Etchegorry, J.P., 2008. 3D modeling of satellite spectral images, radiation budget and energy budget of urban landscapes. Meteorology and Atmospheric Physics 102. https://doi.org/10.1007/s00703-008-0344-1

Gastellu-Etchegorry, J.P., Demarez, V., Pinel, V., Zagolski, F., 1996. Modeling radiative transfer in heterogeneous 3-D vegetation canopies. Remote Sens Environ 58. https://doi.org/10.1016/0034-4257(95)00253-7

Gastellu-Etchegorry, J.P., Grau, E., Lauret, N., 2012. DART: A 3D Model for Remote Sensing Images and Radiative Budget of Earth Surfaces, in: Modeling and Simulation in Engineering. https://doi.org/10.5772/31315

Gastellu-Etchegorry, J.P., Martin, E., Gascon, F., 2004. DART: a 3D model for simulating satellite images and studying surface radiation budget. Int J Remote Sens 25, 73–96. https://doi.org/10.1080/0143116031000115166

Hakala, T., Markelin, L., Honkavaara, E., Scott, B., Theocharous, T., Nevalainen, O., Näsi, R., Suomalainen, J., Viljanen, N., Greenwell, C., Fox, N., 2018. Direct reflectance measurements

from drones: Sensor absolute radiometric calibration and system tests for forest reflectance characterization. Sensors (Switzerland) 18. https://doi.org/10.3390/s18051417

Honkavaara, E., Rosnell, T., Oliveira, R., Tommaselli, A., 2017. Band registration of tuneable frame format hyperspectral UAV imagers in complex scenes. ISPRS Journal of Photogrammetry and Remote Sensing 134. https://doi.org/10.1016/j.isprsjprs.2017.10.014

Honkavaara, E., Saari, H., Kaivosoja, J., Pölönen, I., Hakala, T., Litkey, P., Mäkynen, J., Pesonen, L., 2013. Processing and assessment of spectrometric, stereoscopic imagery collected using a lightweight UAV spectral camera for precision agriculture. Remote Sens (Basel) 5. https://doi.org/10.3390/rs5105006

Jacquemoud, S., Verhoef, W., Baret, F., Bacour, C., Zarco-Tejada, P.J., Asner, G.P., François, C., Ustin, S.L., 2009. PROSPECT + SAIL models: A review of use for vegetation characterization. Remote Sens Environ 113. https://doi.org/10.1016/j.rse.2008.01.026

Janoutová, R., Homolová, L., Malenovskỳ, Z., Hanuš, J., Lauret, N., Gastellu-Etchegorry, J.P., 2019. Influence of 3D spruce tree representation on accuracy of airborne and satellite forest reflectance simulated in DART. Forests 10. https://doi.org/10.3390/f10030292

Kirby, K.J., Bazely, D.R., Goldberg, E.A., Hall, J.E., Isted, R., Perry, S.C., Thomas, R.C., 2014. Changes in the tree and shrub layer of WythamWoods (Southern England) 1974-2012: Local and national trends compared. Forestry 87. https://doi.org/10.1093/forestry/cpu026

Kneubuhler, M., Schaepman, M., Thome, K., Baret, F., Muller, A., 2002. Calibration and Validation of Envisat MERIS Part 1: Vicarious Calibration at Rail Road Valley Playa (NV). Proceedings of MERIS level 2 validation workshop, ESRIN, Frascati, Italy, December 9 13.

Li, W., Guo, Q., Tao, S., Su, Y., 2018. VBRT: A novel voxel-based radiative transfer model for heterogeneous three-dimensional forest scenes. Remote Sens Environ 206. https://doi.org/10.1016/j.rse.2017.12.043

Liu, C., Calders, K., Meunier, F., Gastellu-Etchegorry, J.P., Nightingale, J., Disney, M., Origo, N., Woodgate, W., Verbeeck, H., 2022. Implications of 3D Forest Stand Reconstruction Methods for Radiative Transfer Modeling: A Case Study in the Temperate Deciduous Forest. Journal of Geophysical Research: Atmospheres 127, e2021JD036175. https://doi.org/10.1029/2021JD036175

Ross, J., 1981. The radiation regime and architecture of plant stands (No. 3). Springer Science &

Business Media. https://doi.org/10.1007/978-94-009-8647-3

Saari, H., Pölönen, I., Salo, H., Honkavaara, E., Hakala, T., Holmlund, C., Mäkynen, J., Mannila, R., Antila, T., Akujärvi, A., 2013. Miniaturized hyperspectral imager calibration and UAV flight campaigns, in: Sensors, Systems, and Next-Generation Satellites XVII. https://doi.org/10.1117/12.2028972

Savill, P., Perrins, C., Kirby, K., Fisher, N., 2011. Wytham Woods: Oxford's Ecological Laboratory, Wytham Woods: Oxford's Ecological Laboratory. https://doi.org/10.1093/acprof:osobl/9780199605187.001.0001

Schneider, F.D., Leiterer, R., Morsdorf, F., Gastellu-Etchegorry, J.P., Lauret, N., Pfeifer, N., Schaepman, M.E., 2014. Simulating imaging spectrometer data: 3D forest modeling based on LiDAR and in situ data. Remote Sens Environ 152. https://doi.org/10.1016/j.rse.2014.06.015

Seidler, R., 2017. Patterns of Biodiversity Change in Anthropogenically Altered Forests ☆, in: Reference Module in Life Sciences. https://doi.org/10.1016/b978-0-12-809633-8.02186-5

Thome, K.J., 2001. Absolute radiometric calibration of Landsat 7 ETM+ using the reflectance-based method. Remote Sens Environ 78. https://doi.org/10.1016/S0034-4257(01)00247-4

Thome, K.J., Arai, K., Tsuchida, S., Biggar, S.F., 2008. Vicarious calibration of ASTER via the reflectance-based approach, in: IEEE Transactions on Geoscience and Remote Sensing. https://doi.org/10.1109/TGRS.2008.928730

Van der Zande, D., Stuckens, J., Verstraeten, W.W., Mereu, S., Muys, B., Coppin, P., 2011. 3D modeling of light interception in heterogeneous forest canopies using ground-based LiDAR data. International Journal of Applied Earth Observation and Geoinformation 13. https://doi.org/10.1016/j.jag.2011.05.005

Wang, Y., Czapla-Myers, J., Lyapustin, A., Thome, K., Dutton, E.G., 2011. AERONET-based surface reflectance validation network (ASRVN) data evaluation: Case study for railroad valley calibration site. Remote Sens Environ 115, 2710–2717. https://doi.org/10.1016/j.rse.2011.06.011

Wang, Y., Lauret, N., Gastellu-Etchegorry, J.P., 2020. DART radiative transfer modelling for sloping landscapes. Remote Sens Environ 247. https://doi.org/10.1016/j.rse.2020.111902

Widlowski, J.L., CÔté, J.F., Béland, M., 2014. Abstract tree crowns in 3D radiative transfer models: Impact on simulated open-canopy reflectances. Remote Sens Environ 142. https://doi.org/10.1016/j.rse.2013.11.016

Widlowski, J.L., Mio, C., Disney, M., Adams, J., Andredakis, I., Atzberger, C., Brennan, J., Busetto, L., Chelle, M., Ceccherini, G., Colombo, R., Côté, J.F., Eenmäe, A., Essery, R., Gastellu-Etchegorry, J.P., Gobron, N., Grau, E., Haverd, V., Homolová, L., Huang, H., Hunt, L., Kobayashi, H., Koetz, B., Kuusk, A., Kuusk, J., Lang, M., Lewis, P.E., Lovell, J.L., Malenovský, Z., Meroni, M., Morsdorf, F., Mõttus, M., Ni-Meister, W., Pinty, B., Rautiainen, M., Schlerf, M., Somers, B., Stuckens, J., Verstraete, M.M., Yang, W., Zhao, F., Zenone, T., 2015. The fourth phase of the radiative transfer model intercomparison (RAMI) exercise: Actual canopy scenarios and conformity testing. Remote Sens Environ 169. https://doi.org/10.1016/j.rse.2015.08.016